APL Materials

RESEARCH ARTICLE | MARCH 01 2024

Local defect and mid-gap state analysis of GaN using monochromated EELS combined with nanodiffraction and atomic-resolution imaging

Shunsuke Yamashita ; Sei Fukushima; Jun Kikkawa ; Ryoji Arai; Yuya Kanitani ; Koji Kimoto ; Yoshihiro Kudo

APL Mater. 12, 031101 (2024)
https://doi.org/10.1063/5.0178995

Local defect and mid-gap state analysis of GaN using monochromated EELS combined with nanodiffraction and atomic-resolution imaging

Cite as: APL Mater. 12, 031101 (2024); doi: 10.1063/5.0178995
Submitted: 29 September 2023 • Accepted: 8 February 2024 •
Published Online: 1 March 2024

Shunsuke Yamashita,[1,a)] Sei Fukushima,[1] Jun Kikkawa,[2] Ryoji Arai,[1] Yuya Kanitani,[1] Koji Kimoto,[2] and Yoshihiro Kudo[1]

AFFILIATIONS

[1] Sony Semiconductor Solutions Corporation, 4-14-1 Asahi-cho, Atsugi, Kanagawa 243-0014, Japan
[2] National Institute for Materials Science, 1-1 Namiki, Tsukuba 305-0044, Japan

[a)] **Author to whom correspondence should be addressed:** Shunsuke.A.Yamashita@sony.com

ABSTRACT

Defects in semiconductor materials significantly impact their inherent properties, making the evaluation of local defects and their energy levels crucial for controlling device performance. With advancements in monochromators, electron energy loss spectroscopy (EELS) combined with scanning transmission electron microscopy (STEM) has emerged as a promising approach for assessing crystal and band structures of semiconductor materials at the nanoscale. However, there is limited experimental research investigating the relationship between actual defective structures in local regions and mid-gap states. In this study, we conducted high-energy resolution EELS (HR-EELS) measurements with an energy resolution of less than 100 meV to detect the mid-gap states of GaN. Various defects were intentionally induced through Ga-ion implantation, and the defect concentration varied in the depth direction. To understand the origin of the mid-gap states, we performed 4D-STEM analysis and atomic-resolution STEM observations. The HR-EELS measurements provided insights into the depth-dependent valence-loss spectra, revealing that the intensities corresponding to mid-gap states gradually increased toward the surface, whereas the slope at the onsets corresponding to interband transition decreased. Furthermore, local structural analysis unveiled the presence of structural disorder and defective structures, indicating the existence of extended defects such as stacking faults and domain boundaries. Observably, these defective structures were abundant near the surface and less pronounced in deeper regions. Based on these experimental findings, we concluded that the variations in valence-loss spectra can be utilized to qualitatively evaluate the crystal imperfections at the nanoscale.

I. INTRODUCTION

Understanding the structures and states of semiconductor materials at the nanoscale is of practical importance because device fabrication processes can induce point defects (vacancies, interstitial/substitutional atoms, etc.) and extended defects (stacking faults, domain boundaries, etc.). For example, charged particles and high-energy particles in plasma processes that are key technologies in microfabrication can induce defects and degrade device performance.[1,2] Thus, evaluating process-induced defects has become increasingly important with recent advances in microfabrication.

Several established methods, such as hard x-ray photoelectron spectroscopy (HAXPES),[3,4] deep-level transient spectroscopy,[5–7] and positron annihilation spectroscopy[8,9] are widely used to detect defects or their energy levels, i.e., mid-gap states, with high sensitivity. However, their low spatial resolution hinders nanoscale evaluations. Electron energy loss spectroscopy (EELS) in transmis-

sion electron microscopy (TEM) is an indispensable technique for elemental and chemical state analysis with high spatial resolution in local regions.[10,11] While measuring bandgap energies from valence-loss spectra was limited primarily due to an energy spread of an electron gun in conventional EELS, evolution of monochromators has improved energy resolution down to the millielectronvolt regime,[12,13] paving the way for evaluating not only bandgap energies but also mid-gap states of various semiconductor materials.[14–16] Previous studies have demonstrated the detection of mid-gap states related to point defects or impurities.[17,18] Thus, high energy resolution EELS (HR-EELS) offers inherent capabilities for nanoscale evaluation of process damage and process-induced defects due to its high spatial and energy resolution. However, further experimental studies are needed to investigate mid-gap states, including their relationship with the number of induced defects and their correspondence with actual defective structures, to enable practical applications.

In this study, we conducted HR-EELS measurements on GaN samples with varying defect concentrations in the depth direction to investigate the characteristics of mid-gap states. To induce defective structures, we utilized a focused ion beam (FIB) system for Ga-ion implantation at an acceleration voltage of 30 kV. Synchrotron HAXPES measurements were performed to verify the formation of mid-gap states. Our investigation focused on the depth-dependent behavior of mid-gap states at the nanoscale, specifically analyzing the intensity and shape of valence-loss spectra. To explore the origins of the induced defective structures at the nano- to atomic scale, we employed scanning transmission electron microscopy (STEM)-based diffractometry and imaging. Based on the results obtained from these experiments, we discuss the relationship between the mid-gap states and the induced defective structures.

II. EXPERIMENTAL METHODS

A. Sample preparation

The sample used in this study was an undoped GaN crystal epitaxially grown on a GaN substrate. Defective structures were intentionally induced by Ga-ion implantation at an acceleration voltage of 30 kV using the FIB system (Helios NanoLab 400S, Thermo Fisher Scientific). The probe current was set to 90 pA, and the total dose was estimated to be ~10^{17} ions/cm^2. No annealing process was conducted to prevent repair of the induced damage. We defined the depth of the crystal surface based on the preservation of the crystal lattice because Ga-ion implantation resulted in the amorphization of the GaN surface. The distribution of induced vacancies was simulated using the Stopping and Range of Ions in Matter (SRIM) software.[19,20] To prepare the TEM sample, we employed the same FIB system at an acceleration voltage of 30 kV and subsequently removed the damaged layers on the thinned surfaces using an Ar ion milling system (Gentle Mill, Technoorg Linda) at an acceleration voltage of 350 V. The thickness of the TEM sample, estimated using the EELS log-ratio method,[21] was ~30 nm.

B. HAXPES

The HAXPES measurements to verify the formation of mid-gap states were conducted at the synchrotron radiation facility SPring-8 (BL16XU). For this purpose, the same GaN crystal that underwent Ga-ion implantation in an area of 1 × 8 mm^2 at an acceleration voltage of 30 kV was utilized. Prior to the measurements, the amorphous layers formed on the surface were removed using a 70% tetramethylammonium hydroxide solution at 70 °C for 5 min. The incident x rays had a beam size of 40 × 40 μm^2 and an energy of 7948 eV. Photoelectron spectra were acquired using a photoelectron analyzer (R4000, Scienta Omicron). The incident x ray had a glancing angle of 5°, and the detection angle of the photoelectron was 85°. The actual measurement range, determined by the spread of x rays on the sample and the limited uptake of the photoelectron analyzer, was ~40 × 500 μm^2. The energy resolution, estimated from the Fermi edge of gold, was 340 meV. Notably, photoelectrons generated at depths up to about 25 nm contributed to ~90% of the photoelectron spectra, considering the estimated mean free path of photoelectrons in GaN to be 10.2 nm. To enable comparison, valence band spectra were acquired in both the implanted and non-implanted regions.

C. HR-EELS

For STEM-EELS measurements, an aberration-corrected TEM (Themis Z, Thermo Fisher Scientific) equipped with a monochromator was employed. The acceleration voltage was set to 30 kV to suppress the Cherenkov radiation.[14] The convergence angle of the focused electron probe was 13.9 mrad, and the probe current was set to 23 pA. EEL spectra were acquired using a Gatan imaging filter system (GIF Quantum ERS) and a charge-coupled device (CCD) camera (UltraScan, Gatan). The energy dispersion was set to 5 meV/ch. To enhance the signal-to-noise ratio of valence-loss spectra, two spectra were acquired almost simultaneously in DualEELS mode: one containing a zero-loss peak (ZLP) and the other without the ZLP but including an onset corresponding to an interband transition. The pixel dwell time was set to 0.5 s/pixel. After energy calibration using ZLPs, the background of valence-loss spectra was subtracted using power-law fittings. The bandgap energies were estimated from the inflection points of onsets in the valence-loss spectra.[15] The energy resolution in the sample region, estimated from the full width at half maximum of the ZLP, was 95 meV, as depicted in Fig. S1.

D. Local structural analysis

For 4D-STEM experiments, the same aberration-corrected TEM with an acceleration voltage of 30 kV was utilized. The convergence angle of the focused electron probe was 7.5 mrad, and the probe current was set to 6 pA. Convergent-beam electron diffraction (CBED) patterns of 512 × 512 pixels were acquired using the same CCD camera. The pixel sizes were set to 1.000 nm/pixel in real space and 0.485 mrad/pixel in reciprocal space. The pixel dwell time was set to 2 μs/pixel. To analyze azimuthally averaged scattering intensities, a customized DigitalMicrograph script was employed.

In addition, an aberration-corrected TEM (JEM-ARM300F, JEOL) operating at an acceleration voltage of 300 kV was used for atomic-resolution STEM observations. The convergence angle of the focused electron probe was 24 mrad, and the probe current was ~20 pA. We simultaneously acquired high-angle annular dark-field (HAADF) images showing Z-contrast[22] and annular bright-field (ABF) images visualizing both Ga and N atomic columns.[23] The

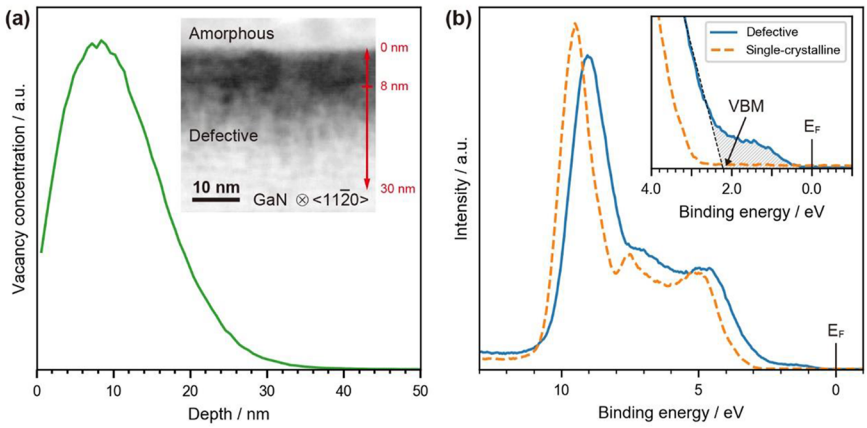

FIG. 1. Details of the Ga-ion implanted GaN. (a) Simulated depth profile of vacancies induced by 30 kV Ga-ion implantation. Inset: BF image acquired along the ⟨11-20⟩ direction near the surface; the red arrow indicates the defective region from surface to depth of 30 nm; the horizontal line represents the depth of 8 nm, where the vacancy concentration is maximum. (b) HAXPES valence band spectra acquired in both the implanted and non-implanted regions. Inset: near-E_F region and shaded region indicate the mid-gap states.

detection angle ranges were 53–175 mrad for HAADF imaging and 11–22 mrad for ABF imaging. To improve the signal-to-noise ratio and reduce image distortion caused by sample drift, customized DigitalMicrograph scripts were employed for multiple fast acquisitions and drift correction.[24,25] The pixel dwell time for each image was set to 5 μs/pixel, and a total of 30 images of size 512 × 512 pixels were acquired. The final HAADF and ABF images were constructed by integrating the drift-corrected images.

III. RESULTS AND DISCUSSION

A. Defect formation by Ga-ion implantation

First, we explain the details of the intentionally damaged GaN through 30 kV Ga-ion implantation. Figure 1(a) presents a simulated depth distribution of vacancies, revealing their presence up to a depth of ~30 nm, with the highest concentration observed at ~8 nm. This distribution serves as a reference for other types of defects. In the inset, a bright-field (BF) image illustrates the distinct contrast variations near the surface, providing visual evidence of defect formation. Figure 1(b) shows the HAXPES valence band spectra in which the blue solid line and the orange dashed line represent the spectra acquired from the implanted (defective) and the non-implanted (single-crystalline) regions, respectively. A peak centered around a binding energy of 9 eV emerged from the photoelectrons originating from the 4*s* orbital of the Ga atoms. The observed shift of ~1 eV in the defective region potentially originates from the shift of the Fermi level (E_F) toward the valence band. The inset focuses on the binding energy range of 0–4 eV, and the position of the valence band maximum (VBM) was estimated through spectrum extrapolation. Notably, a significant increase in signal intensity was observed at ~2 eV between the VBM and E_F in the defective region. The spectrum encompasses signals associated with nearly all defects formed from the surface to a depth of ~25 nm. These results clearly demonstrate the intentional induction of mid-gap states through Ga-ion implantation.

B. Nanoscale evaluation of mid-gap states

Herein, we focus on the detection of mid-gap states at the nanoscale through EEL spectrum imaging. Note that although the HAXPES assessed the mid-gap states between the VBM and E_F, the HR-EELS evaluated the mid-gap states across the entire energy gap. Figure 2(a) displays an ADF image acquired simultaneously with the EEL spectrum imaging data, whereas Fig. 2(b) shows the valence-loss spectra at various depths indicated by arrows in Fig. 2(a). To enhance the signal-to-noise ratios, these spectra were integrated using 12 pixels in the transverse direction and four pixels in the depth direction. As a reference spectrum, the average of spectra #10 and #11 was utilized because the number of defects induced by Ga-ion implantation can be considered negligible beyond a depth of 30 nm. The shaded regions in the spectra represent the intensity increase compared to the reference spectrum, clearly demonstrating the presence of intensified signals throughout the energy gap. This occurrence can be attributed to the induction of various defects in the sample, wherein the EEL spectra encompassed the transitions from the valence band to unoccupied mid-gap states as well as transitions from occupied mid-gap states to the conduction band.[17] Notably, the intensity below 1.2 eV increased toward the surface, revealing the existence of unoccupied mid-gap states between the E_F and the conduction band minimum (CBM). Note that this information is not available with HAXPES in principle. Figure 2(c) illustrates the integrated intensities of the shaded regions, which correspond to the quantity of mid-gap states at each depth. This result establishes that the number of mid-gap states varies with depth, with a greater abundance formed toward the surface.

Another possible interpretation of the intensified signals throughout the energy gap is modulation by factors other than

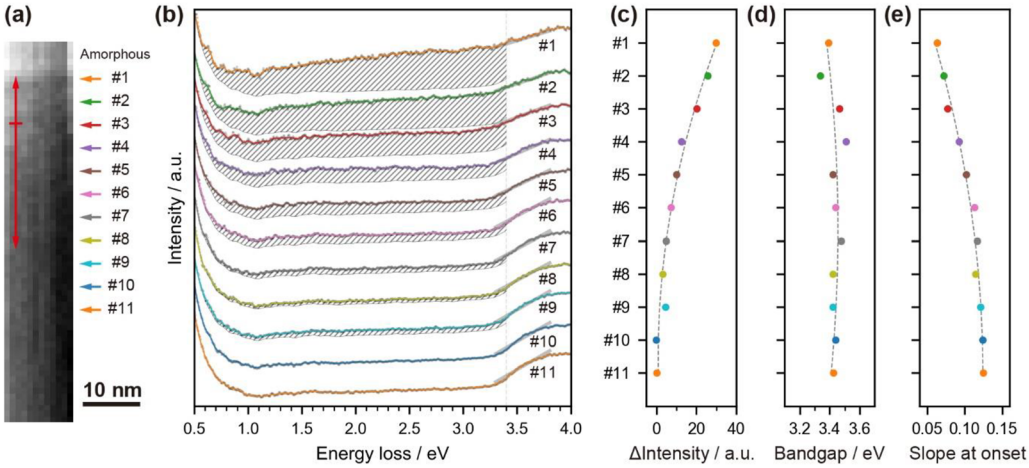

FIG. 2. Depth-dependent EEL spectra of Ga-ion implanted GaN. (a) ADF image acquired simultaneously with the EEL spectrum imaging data. (b) Depth-dependent valence-loss spectra after background subtraction. Solid lines superimposed on the spectra were obtained by Savitzky–Golay smoothing. Intensities below energy loss of 1 eV were caused by the inaccuracies of background subtraction. Depth dependence of (c) integrated intensities corresponding to mid-gap states [ΔIntensity, shaded regions in (b)], (d) bandgap energies, and (e) slope at onsets ~3.4 eV.

defects, such as the retardation effect[26] and the optical waveguide modes.[27,28] However, the effects of Cherenkov radiation and waveguide mode excitation are considered negligible for the following reasons. First, Cherenkov radiation, which is reported to be observable if the electron energy is above 40 keV and sample thickness exceeds 100 nm for GaN,[26] is suppressed for slow electrons with an energy of 30 keV and the sufficiently thin sample of 30 nm thickness in this study. Second, the excitation of waveguide modes is also suppressed for the thin sample with a planar geometry.[27,28] Third, because we focused on the difference from the reference spectrum acquired in the defect-free region deeper than 30 nm, we can exclude the effect of the waveguide mode excitation even if it exists. Therefore, we think that the contribution from various defects dominates the intensified signals in the energy gap region in the valence-loss spectra near the surface.

The distribution of mid-gap states depicted in Fig. 2(c) appears distinct from that depicted in Fig. 1(a), possibly because of the mid-gap states resulting from factors other than vacancies. As displayed in Fig. 2(d), the bandgap energies, estimated from the inflection points of the onsets around 3.4 eV, align with the interband transition of GaN. These bandgap energies exhibited no depth dependence, yielding an average value of 3.43 eV. Figure 2(e) demonstrates the slope at the onsets, determined through linear fitting within the range of 3.3–3.8 eV. Notably, the slope diminished toward the surface, suggesting that structural disorder became more prominent in the vicinity of the surface because structural disorder in materials is known to form band tail states in the forbidden energy gap near the conduction or valence bands.[29–31]

C. 4D-STEM analysis of structural disorder

To delve into the origin of the observed mid-gap states, an analysis of depth-dependent crystallinity was conducted using 4D-STEM, which offers insights into structural disorder. Figure 3(a) shows the ADF image acquired simultaneously with the CBED patterns. Figure 3(b) displays the representative CBED patterns, specifically virtual selected area diffraction patterns, captured from the amorphous, defective, and single-crystalline regions. The amorphous region exhibited a halo pattern with a solitary direct disk, whereas the defective and single-crystalline regions displayed diffraction disks attributed to the GaN crystal. Compared with the single-crystalline region, the diffraction disk intensities were weaker in the defective region, and the background intensity between the disks was heightened. These observations suggest alterations in the crystal structure or crystallinity. For a more detailed comparison, Fig. 3(c) presents the azimuthally averaged scattering intensities obtained from the CBED patterns, including the diffraction peaks of the GaN crystal at an acceleration voltage of 30 kV. In the defective region, a decrease in diffraction intensity within the 15–35 mrad range and an increase in high-angle scattering intensity above 40 mrad were evident. Figure 3(d) illustrates the depth-dependent variation in the diffraction intensity within the 15–35 mrad range. This outcome indicates a gradual decline in diffraction intensity toward the surface, approaching levels comparable to those in the amorphous region near the surface. The increase in high-angle scattering intensity cannot be attributed to an increase in Ga atoms caused by Ga-ion implantation because x-ray energy dispersive spectroscopy (XEDS) depicted in Fig. S2 revealed a slight decrease in Ga content near the surface compared to the single-crystal region. Typically, Bragg scattering originated from periodic structures of crystals, while disorder in periodic structures results in diffuse scattering extending to high angles. Thus, the decrease in diffraction intensity and the increase in diffuse scattering can be attributed to structural disorder. Further support for structural disorder in the defective region is provided by virtual STEM (vSTEM) and virtual dark-field (vDF) imaging (detailed in Fig. S3). Thus, the distribution

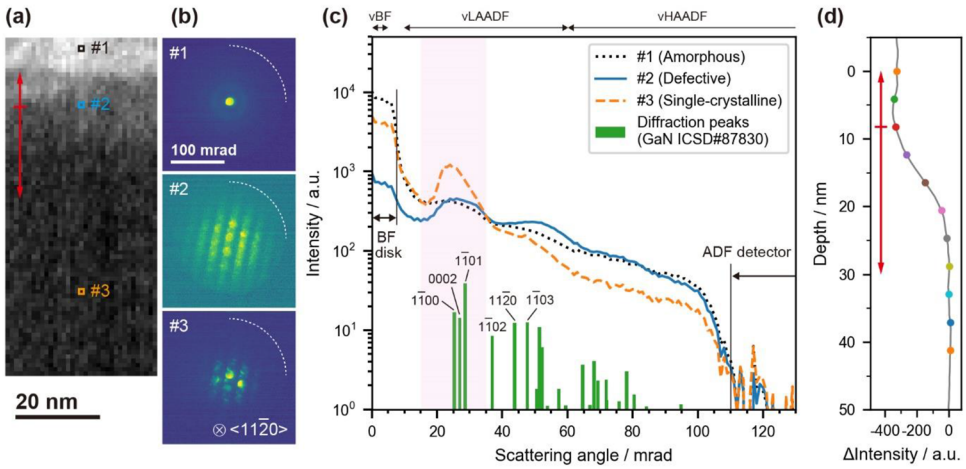

FIG. 3. Depth-dependent crystallinity of the Ga-ion implanted GaN. (a) ADF image acquired simultaneously with CBED patterns. (b) Representative CBED patterns in amorphous (#1), defective (#2), and single-crystalline (#3) regions. The white dotted lines correspond to the inner rim of the physical ADF detector, and no high-angle scattered electrons above 110 mrad were detected. (c) Azimuthally averaged scattering intensities of each CBED pattern in (b). Diffraction peaks of the GaN crystal are displayed for comparison. (d) Depth-dependent diffraction intensities (15–35 mrad), where the intensities were expressed as the difference from the intensity in the single-crystalline region.

of scattering intensity variation offers evidence of depth-dependent structural disorder in the defective region.

D. Atomic-resolution STEM observation of defective structures

Subsequently, atomic-resolution STEM images were acquired to examine the actual structures within the defective region. Figures 4(a)–4(d) present the pairs of HAADF and ABF images acquired in different regions near the surface, respectively. Several characteristic structures, including stacking faults (SFs) and inversion domains (IDs), were observed. Figure 4(e) shows the structural models that could account for the observed defective structures. The same models were superimposed on the corresponding sections of the ABF images in Figs. 4(b) and 4(d). Each observed defective structure had a width of ~5–10 nm, corresponding to the grains visualized in the vDF images depicted in Fig. S3. The prevalence of defective structures at a depth of around 30 nm was clearly lower than that near the surface, as depicted in Fig. S4. Although complete identification of point defects using projected images of three-dimensional structures is challenging owing to the negligible contrast variations, we speculate the presence of various point defects other than vacancies. These atomic-resolution STEM observations demonstrate the existence of crystal imperfections, including various extended defects.

In this paragraph, we describe the relationship between the observed defective structures and the mid-gap states. In SF#1, the stacking sequence along the [0001] direction shifts from *BABAB*. . . for the wurtzite (WZ) structure to *CABC*. . . for the zinc blende (ZB) structure. Previous studies have reported that the WZ/ZB interface induces a mid-gap state at an energy 0.13 eV above the VBM[32] or offsets the conduction and valence bands, forming a shallow quantum well-like structure.[33] Common to SF#2, #3, and #4, dumbbell structures were observed, where two Ga atomic columns were aligned in the ⟨1-100⟩ direction, as indicated by the red dotted area in Fig. 4(e). This can be explained by a structure in which both sides of the stacking misfit boundaries (SMBs), also known as double positioning boundaries, overlap along the ⟨11-20⟩ direction.[34,35] Assuming the presence of SMBs, a mid-gap state with an energy of 1.1 eV above the VBM is induced.[35] Furthermore, SF#3 involves an overlap between a WZ structure and a type I_1 SF along the ⟨11-20⟩ direction. Type I_1 SFs are the most easily formed among SFs in WZ structures due to their low formation energy,[33,36] and the associated dislocations induce mid-gap states within the energy range of 2 eV above the VBM and at positions 0.7 eV below the CBM and 1.8 eV above the VBM.[37] The regions indicated by ID can be explained by the overlapping of polarity-inversion domains along the ⟨11-20⟩ direction.[38,39] For ID (Ga) and ID (N), the inversion domains are shifted in the [0001] direction, aligning the Ga or N atomic columns with the same atomic columns in the original domains, respectively. A theoretical study has reported that inversion domain boundaries do not induce mid-gap states.[35]

E. Relationship between mid-gap states and defective structures

Finally, we summarize the relationship between the mid-gap states and the defective structures. Figure 5(a) presents a schematic diagram of Ga-ion implanted GaN, illustrating the distribution of point defects (vacancies, interstitial/substitutional atoms, etc.) and extended defects (stacking faults, domain boundaries, etc.) based on the simulation results in Fig. 1(a) and STEM observations in Fig. 4. For comparison, the vDF image reconstructed using the 0002 disk from the 4D-STEM dataset is portrayed as well. Figure 5(b) depicts the density of states, showing the energy levels of the mid-gap states

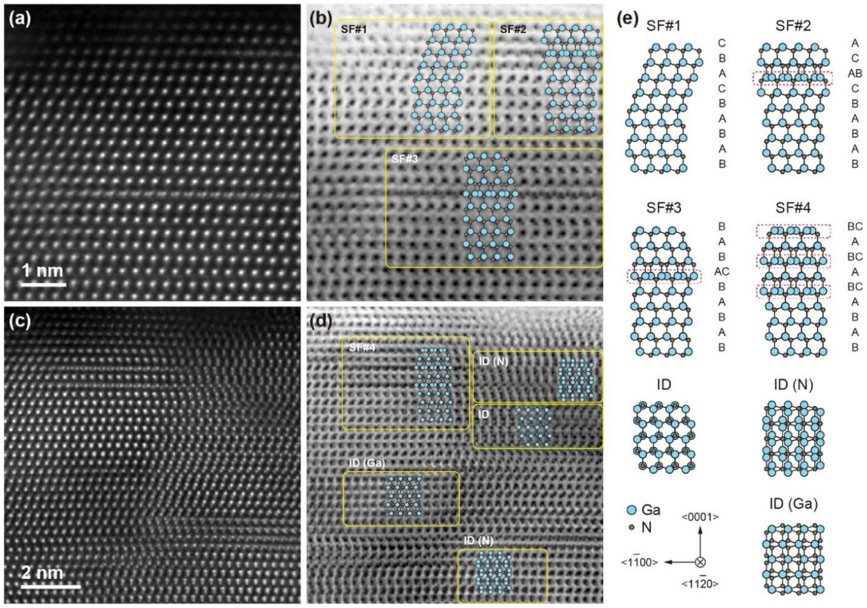

FIG. 4. Defective structures of the Ga-ion implanted GaN. (a) and (b) HAADF and ABF images acquired near the surface. (c) and (d) HAADF and ABF images acquired near the surface but in another region. These images were acquired along the ⟨11-20⟩ zone-axis direction. (e) Schematic of projected structural models containing SFs or IDs. Stacking sequence along the [0001] direction is depicted in each model.

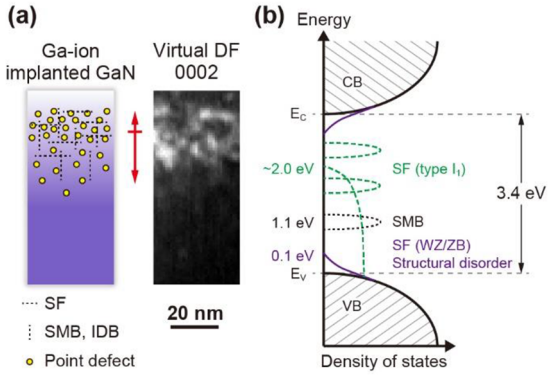

FIG. 5. (a) Schematic of the Ga-ion implanted GaN and the vDF image reconstructed using the 0002 disk. (b) Density of states displaying the energy level of each mid-gap state induced by crystal imperfections.

induced by the observed crystal imperfections. The combination of structural disorder, extended defects, and various (unspecified) point defects potentially contributed to the formation of mid-gap states throughout the energy gap. Although the position-averaged E_F can be estimated from the HAXPES valence band spectrum shown in Fig. 1(b), the actual position of E_F depends on the local defective structures and cannot be explicitly depicted in Fig. 5(b). This interpretation aligns with the HAXPES and HR-EELS results that demonstrated the presence of occupied mid-gap states between VBM and E_F and unoccupied mid-gap states between E_F and CBM, respectively. Therefore, based on these findings, we conclude that the variations in the valence-loss spectra in Fig. 2 qualitatively reflect the depth-dependent crystal imperfections in GaN induced by Ga-ion implantation.

IV. CONCLUSIONS

In summary, we conducted HR-EELS measurements and performed STEM-based local structural analysis to explore the relationship between mid-gap states and defective structures in GaN intentionally damaged by Ga-ion implantation. We discovered that the mid-gap states and defective structures exhibited a similar depth dependence, and the intensities and shapes of the valence-loss spectra qualitatively reflected the crystal imperfections, including the structural disorder and extended defects. HR-EELS holds promise for the nanoscale evaluation of various defects that may arise in the development of advanced semiconductor materials and devices because it has the potential to detect point defects and structural disorder that are challenging to detect using conventional STEM observations. One limitation of this study is the absence of a quantitative discussion on the defect concentration. Further investigations on detection limits using samples with controlled defect concentrations are crucial for clarifying the application scope of HR-EELS in the nanoscale evaluation of crystal imperfections.

SUPPLEMENTARY MATERIAL

The supplementary material contains the comparison of ZLPs and valence-loss spectra collected with and without monochromators, depth profiles of the characteristic X-ray intensities of Ga K and N K emissions, virtual images reconstructed from the 4D-STEM dataset, and HAADF/ABF images acquired at the depth of about 30 nm.

ACKNOWLEDGMENTS

The synchrotron radiation experiments were performed at the BL16XU of SPring-8 with the approval of the Japan Synchrotron Radiation Research Institute (JASRI) (Proposal No. 2021A5040).

AUTHOR DECLARATIONS

Conflict of Interest

The authors have no conflicts to disclose.

Author Contributions

The manuscript was written through the contributions of all authors. All authors have given approval for the final version of the manuscript.

Shunsuke Yamashita: Formal analysis (equal); Investigation (equal); Software (lead); Writing – original draft (lead); Writing – review & editing (equal). **Sei Fukushima**: Formal analysis (equal); Investigation (equal); Writing – review & editing (equal). **Jun Kikkawa**: Investigation (equal); Writing – review & editing (equal). **Ryoji Arai**: Formal analysis (equal); Investigation (equal); Writing – review & editing (equal). **Yuya Kanitani**: Writing – review & editing (equal). **Koji Kimoto**: Writing – review & editing (equal). **Yoshihiro Kudo**: Writing – review & editing (equal).

DATA AVAILABILITY

The data that support the findings of this study are available from the corresponding author upon reasonable request.

REFERENCES

[1]K. Eriguchi and K. Ono, "Quantitative and comparative characterizations of plasma process-induced damage in advanced metal-oxide-semiconductor devices," J. Phys. D: Appl. Phys. **41**(2), 024002 (2008).
[2]K. Eriguchi, "Defect generation in electronic devices under plasma exposure: Plasma-induced damage," Jpn. J. Appl. Phys. **56**(6S2), 06HA01 (2017).
[3]C. Weiland, A. K. Rumaiz, P. Pianetta, and J. C. Woicik, "Recent applications of hard x-ray photoelectron spectroscopy," J. Vac. Sci. Technol. A **34**(3), 030801 (2016).
[4]M. Sumiya, S. Ueda, K. Fukuda, Y. Asai, Y. Cho, L. Sang, A. Uedono, T. Sekiguchi, T. Onuma, and T. Honda, "Valence band edge tail states and band gap defect levels of GaN bulk and $In_xGa_{1-x}N$ films detected by hard X-ray photoemission and photothermal deflection spectroscopy," Appl. Phys. Express **11**(2), 021002 (2018).
[5]D. V. Lang, "Deep-level transient spectroscopy: A new method to characterize traps in semiconductors," J. Appl. Phys. **45**(7), 3023–3032 (1974).
[6]Y. Tokuda, "(Invited) DLTS studies of defects in n-GaN," ECS Trans. **75**(4), 39–49 (2016).
[7]P. Hacke, T. Detchprohm, K. Hiramatsu, N. Sawaki, K. Tadatomo, and K. Miyake, "Analysis of deep levels in *n*-type GaN by transient capacitance methods," J. Appl. Phys. **76**(1), 304–309 (1994).
[8]A. Uedono, S. Ishibashi, N. Oshima, and R. Suzuki, "Positron annihilation spectroscopy on nitride-based semiconductors," Jpn. J. Appl. Phys. **52**(8S), 08JJ02 (2013).
[9]A. Uedono, T. Watanabe, S. Kimura, Y. Zhang, M. Lozac'h, L. Sang, S. Ishibashi, N. Oshima, R. Suzuki, and M. Sumiya, "Vacancy-type defects in $In_xGa_{1-x}N$ grown on GaN templates probed using monoenergetic positron beams," J. Appl. Phys. **114**(18), 184504 (2013).
[10]R. F. Egerton, *Electron Energy-Loss Spectroscopy in the Electron Microscope* (Springer, Boston, MA, 2011).
[11]H. Yamamoto, K. Tanaka, S. Tomiya, S. Yamashita, M. Ukita, H. Nakano, R. Shirasawa, M. Kotera, and K. Funatsu, "Dry etching damage and alloy composition analysis of GaN-based semiconductors using electron energy-loss spectroscopy," J. Electron. Mater. **50**(7), 4230–4237 (2021).
[12]K. Kimoto, "Practical aspects of monochromators developed for transmission electron microscopy," Microscopy **63**(5), 337–344 (2014).
[13]O. L. Krivanek, N. Dellby, J. A. Hachtel, J.-C. Idrobo, M. T. Hotz, B. Plotkin-Swing, N. J. Bacon, A. L. Bleloch, G. J. Corbin, M. V. Hoffman, C. E. Meyer, and T. C. Lovejoy, "Progress in ultrahigh energy resolution EELS," Ultramicroscopy **203**, 60–67 (2019).
[14]L. Gu, V. Srot, W. Sigle, C. Koch, P. van Aken, F. Scholz, S. B. Thapa, C. Kirchner, M. Jetter, and M. Rühle, "Band-gap measurements of direct and indirect semiconductors using monochromated electrons," Phys. Rev. B **75**(19), 195214 (2007).
[15]J. Lin, L. Gomez, C. de Weerd, Y. Fujiwara, T. Gregorkiewicz, and K. Suenaga, "Direct observation of band structure modifications in nanocrystals of $CsPbBr_3$ perovskite," Nano Lett. **16**(11), 7198–7202 (2016).
[16]T. Asano, M. Tezura, M. Saitoh, H. Tanaka, J. Kikkawa, and K. Kimoto, "Nanoscale observation of subgap excitations in β-Si_3N_4 with a high refractive index using low-voltage monochromated STEM: A new approach to analyze the physical properties of defects in dielectric materials," Appl. Phys. Express **15**(7), 076501 (2022).
[17]W. J. Bowman, K. March, C. A. Hernandez, and P. A. Crozier, "Measuring bandgap states in individual non-stoichiometric oxide nanoparticles using monochromated STEM EELS: The Praseodymium–ceria case," Ultramicroscopy **167**, 5–10 (2016).
[18]S. Wang, K. March, F. A. Ponce, and P. Rez, "Identification of point defects using high-resolution electron energy loss spectroscopy," Phys. Rev. B **99**(11), 115312 (2019).
[19]J. P. Biersack and L. G. Haggmark, "A Monte Carlo computer program for the transport of energetic ions in amorphous targets," Nucl. Instrum. Methods **174**(1–2), 257–269 (1980).
[20]J. F. Ziegler, M. D. Ziegler, and J. P. Biersack, "SRIM—The stopping and range of ions in matter (2010)," Nucl. Instrum. Methods Phys. Res. B. **268**(11–12), 1818–1823 (2010).
[21]T. Malis, S. C. Cheng, and R. F. Egerton, "EELS log-ratio technique for specimen-thickness measurement in the TEM," J. Electron Microsc. Tech. **8**(2), 193–200 (1988).
[22]S. Yamashita, J. Kikkawa, K. Yanagisawa, T. Nagai, K. Ishizuka, and K. Kimoto, "Atomic number dependence of *Z* contrast in scanning transmission electron microscopy," Sci. Rep. **8**(1), 12325 (2018).
[23]S. D. Findlay, N. Shibata, H. Sawada, E. Okunishi, Y. Kondo, and Y. Ikuhara, "Dynamics of annular bright field imaging in scanning transmission electron microscopy," Ultramicroscopy **110**(7), 903–923 (2010).
[24]K. Kimoto, R.-J. Xie, Y. Matsui, K. Ishizuka, and N. Hirosaki, "Direct observation of single dopant atom in light-emitting phosphor of β-SiAlON:Eu^{2+}," Appl. Phys. Lett. **94**(4), 041908 (2009).
[25]S. Yamashita, S. Koshiya, T. Nagai, J. Kikkawa, K. Ishizuka, and K. Kimoto, "Quantitative annular dark-field imaging of single-layer graphene-II: Atomic-resolution image contrast," Microscopy **64**(6), 409–418 (2015).

[26]R. Erni and N. D. Browning, "The impact of surface and retardation losses on valence electron energy-loss spectroscopy," Ultramicroscopy **108**(2), 84–99 (2008).
[27]N. D. Browning, I. Arslan, R. Erni, and B. W. Reed, Low-loss EELS in the STEM, in: S. J. Pennycook and P. D. Nellist (Eds.), *Scanning Transmission Electron Microscopy* (Springer, New York, 2011), pp. 685–688.
[28]I. Arslan, J. K. Hyun, R. Erni, M. N. Fairchild, S. D. Hersee, and D. A. Muller, "Using electrons as a high-resolution probe of optical modes in individual nanowires," Nano Lett. **9**(12), 4073–4077 (2009).
[29]F. Urbach, "The long-wavelength edge of photographic sensitivity and of the electronic absorption of solids," Phys. Rev. **92**(5), 1324 (1953).
[30]V. S. Olsen, G. Baldissera, C. Zimmermann, C. S. Granerød, C. Bazioti, A. Galeckas, B. G. Svensson, A. Yu Kuznetsov, C. Persson, Ø. Prytz, and L. Vines, "Evidence of defect band mechanism responsible for band gap evolution in $(ZnO)_{1-x}(GaN)_x$ alloys," Phys. Rev. B **100**(16), 165201 (2019).
[31]J. F. Wager, "Real- and reciprocal-space attributes of band tail states," AIP Adv. **7**(12), 125321 (2017).
[32]Z. Z. Bandić, T. C. McGill, and Z. Ikonić, "Electronic structure of GaN stacking faults," Phys. Rev. B **56**(7), 3564–3566 (1997).
[33]C. Stampfl and C. G. van de Walle, "Energetics and electronic structure of stacking faults in AlN, GaN, and InN," Phys. Rev. B **57**(24), R15052–R15055 (1998).
[34]C. Bazioti, A. Azarov, K. M. Johansen, B. G. Svensson, L. Vines, A. Y. Kuznetsov, and Ø. Prytz, "Role of nitrogen in defect evolution in zinc oxide: STEM–EELS nanoscale investigations," J. Phys. Chem. Lett. **10**(16), 4725–4730 (2019).
[35]J. E. Northrup, J. Neugebauer, and L. T. Romano, "Inversion domain and stacking mismatch boundaries in GaN," Phys. Rev. Lett. **77**(1), 103–106 (1996).
[36]K. Dovidenko, S. Oktyabrsky, and J. Narayan, "Characteristics of stacking faults in AlN thin films," J. Appl. Phys. **82**(9), 4296–4299 (1997).
[37]J. Kioseoglou, E. Kalesaki, L. Lymperakis, J. Neugebauer, P. Komninou, and T. Karakostas, "Electronic structure of 1/6⟨2023⟩ partial dislocations in wurtzite GaN," J. Appl. Phys. **109**(8), 083511 (2011).
[38]S. Mohn, N. Stolyarchuk, T. Markurt, R. Kirste, M. P. Hoffmann, R. Collazo, A. Courville, R. Di Felice, Z. Sitar, P. Vennéguès, and M. Albrecht, "Polarity control in group-III nitrides beyond pragmatism," Phys. Rev. Appl. **5**(5), 054004 (2016).
[39]N. Stolyarchuk, T. Markurt, A. Courville, K. March, J. Zúñiga-Pérez, P. Vennéguès, and M. Albrecht, "Intentional polarity conversion of AlN epitaxial layers by oxygen," Sci. Rep. **8**(1), 14111 (2018).